Fabrication of 3D printed hollow microneedles by Digital Light Processing (DLP) for the buccal delivery of actives

Journal:	*ACS Biomaterials Science & Engineering*
Manuscript ID	ab-2023-00116h
Manuscript Type:	Article
Date Submitted by the Author:	27-Jan-2023
Complete List of Authors:	Monou, Paraskevi-Kyriaki; Aristotle University of Thessaloniki, Department of Pharmacy Andriotis, Eleftherios; Aristotle University of Thessaloniki Tsongas, Konstantinos ; International Hellenic University Tzimtzimis , Emmanuel ; International Hellenic University Katsamenis, Orestis; University of Southampton Tzetzis, Dimitrios; International Hellenic University School of Science and Technology Anastasiadou, Pinelopi ; Aristotle University of Thessaloniki Vizirianakis, Ioannis; Aristotle University of Thessaloniki, Pharmaceutical Sciences Andreadis, Dimitrios; Aristotle University of Thessaloniki Fatouros, Dimitrios; Aristotle University of Thessaloniki, School of Pharmacy

Fabrication of 3D printed hollow microneedles by Digital Light Processing (DLP) for the buccal delivery of actives

Paraskevi Kyriaki Monou[1,2], Eleftherios G. Andriotis[1], Konstantinos Tsongas[3,4], Emmanouil K. Tzimtzimis[3] Orestis L. Katsamenis[5], Dimitrios Tzetzis[3], Pinelopi Anastasiadou[6], Ioannis S. Vizirianakis[2,7,8], Dimitrios Andreadis[5], Dimitrios G. Fatouros[1,2,]*

[1]Department of Pharmacy Division of Pharmaceutical Technology, Aristotle University of Thessaloniki, Thessaloniki 54124, Greece;

[2]Center for Interdisciplinary Research and Innovation (CIRI-AUTH), 57001 Thessaloniki, Greece

[3] Digital Manufacturing and Materials Characterization Laboratory, International Hellenic University, School of Science and Technology, Thessaloniki57001, Greece;

[4]Department of Industrial Engineering and Management, International Hellenic University, 57001 Thessaloniki, Greece;

[5]μ-VIS X-ray Imaging Centre, Faculty of Engineering and Physical Sciences, University of Southampton, Southampton, United Kingdom; SO17 1BJ, UK

[6]Department of Oral Medicine/Pathology, School of Dentistry, Aristotle University of Thessaloniki, Thessaloniki 54124, Greece;

[7]Department of Pharmacy, Laboratory of Pharmacology, Aristotle University of Thessaloniki, 54124 Thessaloniki, Greece;

[8]Department of Life and Health Sciences, University of Nicosia, CY-1700 Nicosia, Cyprus

KEYWORDS

Microneedles, hollow, buccal delivery, 3D printing, macromolecules, Digital Light Processing (DLP), microfocus Computed Tomography (μCT)

ABSTRACT

In the present study, two different microneedle devices were produced using Digital Light Processing (DLP). Two different shapes of needles namely; hexagonal and syringe-like needles were evaluated regarding their mechanical properties and their ability to penetrate the buccal mucosa to effectively deliver actives with molecular weight between 600 – 4000 Da. Attached reservoirs were designed and printed along with the arrays as a whole device. Light microscopy was used to quality control the printability of the designs, whereas non-destructive volume imaging by means of microfocus Computed Tomography (μCT) was employed for dimensional- and defect characterisation of the DLP printed devices. The buccal tissue penetration process was studied using penetration test and finite element (FE) analysis, which showed that maximum stress experienced by the needles during the insertion process was below their ultimate compressive strength. Permeation studies showed the increased permeability of two model drugs when delivered with the MN devices. The safety of these printed devices for buccal administration was confirmed by histological evaluation and cell viability studies using TR146 cell line.

Introduction

The buccal mucosa has been widely explored for drug delivery because of its large surface, high permeability, and rapid repair [1]. Buccal route of delivery offers many advantages such as avoiding first-pass effect, avoiding protein destruction by gastric enzymes, and enhanced patient compliance[2]. Moreover, both local and systemic treatment can be applied with the buccal administration of drugs [3]. Many dosage forms have been produced for buccal applications, including films [4], tablets [5], nanoparticles [6], and gels [7].

Microneedles (MNs) for buccal applications have been explored for applications like vaccination and the delivery of macromolecules like insulin [8,9]. MNs were first introduced for transdermal delivery of active pharmaceutical ingredients (APIs) such as hormones[10], vaccines[11], antibiotics[12], and glucocorticoids[13]. Buccal MN arrays are promising for the effective treatment using peptides and proteins. Dosing proteins through the oral route is impossible since they degrade in the gastrointestinal tract and have low membrane permeability. Their administration is limited to the parenteral routes which cause fear and discomfort to patients, mainly in the paediatric and geriatric populations [2]. Different types of MNs were fabricated for skin delivery including solid, hollow, and coated MNs[14], using techniques like laser cutting, laser ablation, electrodeposition, lithography, etching, and micromolding as manufacturing processes[15]. Additive manufacturing (AM), a newly introduced technology, has also been employed for MN fabrication[16].

AM and 3D printing, in particular, allow the layer-by-layer manufacturing of complex 3D structures with high precision[17]. Compared to the traditional fabrication processes, 3D printing controls the topological diversity of the MN arrays and it is cost-efficient as a one-step procedure[18]. Digital Light Processing (DLP) 3D printing is based on photopolymerization of a liquid resin to create solid objects with high resolution and accuracy, compared to other 3D printing techniques[19,20]. Thus, it is the most appropriate 3D printing process for the production of MN arrays as DLP provides the opportunity to construct objects with microscopic features such as micron-sized needles (< 1000 μm) and their elaborate shapes (e.g. cone[21], pyramid[22], syringe-like[23]). 3D printing of MNs has recently emerged in the field, offering new potential to the transdermal and buccal drug delivery market, based on the unique asset of 3D printing, the easy and fast customization. 3D printing promotes personalized therapy and enables the flexibility to develop on-demand devices, fully adapted to the patient’s needs. Moreover, this customization is cost-effective, and fast, allowing multifunctional treatment by combining more than one APIs in a single device[16].

Both solid and hollow MNs have been developed using 3D printing technologies. Their production is mostly based on vat photopolymerization, namely Stereolithography (SLA), Digital Light Processing (DLP), Two-Photon Polymerization (2-TPP), Liquid-Crystal Display (LCD) and Digital Light Processing (DLP). Generally, most of the above technologies have been employed for transdermal MN patches or devices. SLA has been used for the production of MNs for transdermal delivery of model dyes[24] and insulin[25]. Transdermal delivery of insulin has also been tested using 3D printed hollow MNs using SLA[23] and LCD[26]. Hollow MNs were also printed with DLP to explore the feasibility of the method and to optimize the critical parameters for the successful fabrication of hollow MN arrays[27]. In addition to these techniques, 2-TPP, the most expensive and accurate 3D printing method [28], has been employed for the production of biocompatible MNs for dermal applications[29] and also the production of MNs with antimicrobial properties[30].

MNs for buccal applications are currently being explored for both local and systemic effects. MN penetration to the buccal tissue seems to be less painful than the other sites of the oral cavity (tongue, palate, gingiva, and lip)[31]. MN patches with topical anesthetics reduced the pain from dental injections by causing minimum discomfort to the patients[32]. Coated MNs with anti-cancer drugs were evaluated for the treatment of oral carcinomas[33]. Moreover, buccal MN patches have been tested for vaccine administration, promoting the immunological response[8,34]. Finally, MN patches for delivering macromolecules have also been reported, suggesting that these drug delivery systems could potentially improve adherence and facilitate drug delivery to the paediatric population[9].

In the present study, two different shapes of MNs were printed using DLP. Attached reservoirs and luer locks were designed and printed as whole devices to facilitate the infusion through the MN channels. These devices hold promise for an array of medicines for special populations like paediatric and geriatric patients[35]. This approach might overcome the pitfalls of the existing methodologies by enhancing the acceptability of medicines, meet the individual needs of patients, mainly children and elders, and hence improve their health. For example, elderly people with swallowing difficulties (dysphagia, xerostomia) due to polypharmacy might miss their medication leading to poor outcomes (worse symptoms) and slow recovery. The current approach can improve medication adherence creating at the same personalized medicine for patients.

Materials and Methods

Materials

Biocompatible Class I resin (Dental SG) was purchased from Formlabs (Somerville, Massachusetts, United States). Isopropyl alcohol (99.9%), fluorescein isothiocyanate–dextran

(FITC-dextran) (MW 4000%Da), calcein (MW 622.54), and thiazolyl blue tetrazolium bromide (MTT) were purchased from Sigma-Aldrich (St. Louis, Missouri, USA). Ham's F12 (with l-glutamine) was purchased from Lonza (Basel, Switzerland). All other reagents were of analytical grade.

Microneedle design and fabrication

The microneedle (MN) arrays (7 x 7) were originally designed using SolidWorks CAD software (Dassault Systemes, SolidWorks Corporation, Waltham, MA, USA) and STL files were created. The CADs used for the FEA simulations were designed using SolidWorks CAD software (Dassault Systemes, SolidWorks Corporation, Waltham, MA, USA). The MNs were designed with two different shapes namely; hexagonal (array I) and syringe-like (array II) needles. Their height was designed to be 700 μm, the layer height was 50 μm and the whole patch was circular with a 20 mm diameter. Attached reservoirs to both arrays were designed and printed as a whole device. The MN devices were fabricated using a DLP printer (XYZ PartPro100 xP, Taiwan) using Dental SG, a biocompatible resin as the printing material. After printing, the MNs were washed out with

Isopropyl Alcohol (15 min) and cured under ultraviolet radiation for 45 min to ensure the full polymerization of the resin.

Microscopy

The 3D printed MNs were visualized using a digital light microscope (Dino-Lite AB7013MZE, AnMo Electronics, Hsinchu, Taiwan) to confirm their shape fidelity and to examine the morphology of the needles. Their dimensions were measured with aid of the software DinoLite 2.0. The MNs were inserted in a charge reduction sample holder and visualized with a Desktop Phenom ProX scanning electron microscope (ThermoFischer, USA)

Mechanical properties

Compression tests were performed in both arrays to evaluate the fracture strength of the MNs. A tensile test machine equipped with a 500 N load cell (M500-50AT Testometric Company, Rochdale, UK) was employed and the arrays were mounted on the metal rod with double adhesive tape. The metal rod was programmed to descend at a speed of 0.5 min/mm onto a metal plate causing the compression failure of the MNs. The compression force was over 300 N, a value much higher than the usual forces a MN array experiences during skin or buccal penetration[24,36].

Volumetric Imaging and characterisation by mean of microfocus Computed Tomography (μCT)

μCT imaging: μCT imaging was conducted to evaluate the volumetric characteristics of the printed objects, with specific focus on the needles. μCT imaging was performed using a customised μCT scanner optimised for 3D X-ray histology (www.xrayhistology.org) based on Nikon's XTH225ST system (Nikon Metrology UK Ltd) at the Biomedical Imaging Unit / University Hospital Southampton. Imaging was conducted at 80 kVp / 125 μA without any beam pre-filtration. A 2850 x 2850 dexels detector was used and the source to detector and source to object distances were 938 mm and 62.5 mm respectively resulting in a voxel size of 15 μm. Imaging parameters were as follows: 2001 projections were collected over the 360° rotation, with 4 frames per projection being averaged for each projection to improve the signal to noise ratio.

Reconstruction of the volume data, image processing and analysis: Following completion of each acquisition, projection data were automatically reconstructed into 32-bit volumes by means of Nikon's own reconstruction engine which uses a filtered-back projection algorithm. Each dataset was then resliced (re-oriented in space) and cropped in using Fiji / ImageJ[37] and the volumes were saved in 8-bit files. Volumetric analysis and visualisation were conducted in "Dragonfly" (v. 2022.1; Object Research Systems (ORS) Inc, Montreal, Canada, 2020; software available at http://www.theobjects.com/dragonfly). The needles from each component were segmented using thresholding and manual refinement. Analysis was conducted using the connected components tool applied on the segmented needle object.

Penetration test using buccal mucosa and Finite Element Analysis (FEA)

Sufficient insertion of the MNs into the buccal tissue is imperative for proper drug delivery. Penetration tests for array 1 and array 2 were conducted using the Testometric tensile machine (Rochdale, UK). Buccal tissue from pigs was collected from a local abattoir and was immediately transferred to the lab for preparation. The tissue was mounted onto a cork plate with pins and the arrays were attached to the moving cylindrical probe using double-sided adhesive tape. The MNs were inserted into the buccal mucosa at a speed of 0.5 mm/min. The experiment was stopped when the load was exerted from the MNs to the buccal tissue. After insertion, the MNs were inspected with a digital microscope to further examine their deformation and their geometric alteration. An explicit dynamics Finite element analysis (FEA) based on the ANSYS code was performed to simulate the behaviour of the microneedles and the buccal tissue during the insertion process. This model will provide an estimation of the stress behaviour of the microneedles under the insertion process, along with the safety factor of the structure.

Permeation studies

Permeation studies were conducted in vertical Franz cells using aqueous solutions of FITC-dextran (1 mg/mL) and calcein (1mg/mL) as model APIs. Porcine buccal mucosa was mounted between the donor and the acceptor. The acceptor was filled with PBS (pH 7.4, 37 ˚C) and the MN devices were placed onto the buccal tissue for 30 and 60 sec at different flow rates using a syringe pump (NE-100, New Era Pump Systems Inc., New York, USA). High flow rates (0.5 - 0.2 mL/min) resulted in the leaking of the solution, thus a flow rate of 0.05 mL/min was selected for the study. The permeation profile was monitored for 4h. The two dyes were quantified by fluorescence spectroscopy (RF-5301-PC Fluorescence Spectrophotometer, Shimadzu, Kyoto, Japan): excitation 490 nm and emission 520 nm.

Histological evaluation

To ensure the safety of the printed MNs and to study the effect of the MN array on the tissue microanatomy, a histological evaluation was performed. Porcine mucosa samples were pierced with array 1 and array 2 for 30 and 60 sec. The samples were fixed in formaldehyde solution and subsequently embedded in paraffin oil. 4 μm thickness sections were taken using a cryostat, stained with hematoxylin eosin dye solutions, and visualized with an optical microscope (Olympus CX31, Olympus, Tokyo, Japan).

Cell viability-MTT assay

Cell viability studies were carried out to investigate the cytotoxic effect of the resin used to produce the MNs. Three printed cubes (1 cm^3) were fabricated with the biocompatible resin and immersed in sterile PBS. 300 μL of PBS extract was removed at predetermined time points (3, 24, and 48h) and split into two parts (100 μL and 200 μL)[38]. Circular discs were also printed and placed in the bottom of the well to examine the cell growth. The cytotoxic effect of the PBS extracts and the printed samples was assessed using the TR146 cell line and the viability was determined with the MTT method. The cells were cultured in DMEM supplemented with 10% FBS and 1%

penicillin/streptomycin (100 U/ml) and seeded in 96-well plates at a density of 10^4 cells/well. After 24h in culture to allow attachment, the cells were treated with the samples in question and incubated at 37 ˚C for additional 24h. At the end of this treatment, the medium was removed and the cells were rinsed with PBS. MTT solution (5mg/mL) was added to the wells for further incubation at 37 ˚C. After 4h, the MTT solution was removed and DMSO was added to dissolve the formazan crystals. Following mild agitation for 15 min, the absorption was measured at 570 nm, using an ELISA plate reader.

Statistical analysis

The results are presented as mean ± SD and all the experiments were conducted in triplicate. Unpaired Student's t-test was applied and statistical significance was indicated by $p < 0.05$.

Results and Discussion

Visual inspection of the printed MN devices with a microscope

Figure 1 depicts the printed MN devices. Reservoirs were designed and printed as a single device. Both reservoirs had attached luers to facilitate the connection between the needles and the liquid containers. Both arrays were printed directly onto the platform. Array I had hexagonal needles (Figure 1) and the reservoir was designed with channels. Needle height, layer height, and tip diameter were measured to be approximately 692 μm, 48 μm, and 119 μm, respectively. Array II was designed with syringe-like needles. Dimensions such as their height, layer height, and tip diameter were approximately 853 μm, 45 μm and 197 μm, respectively. All the dimensions were in good agreement with the CAD model, demonstrating the good printability of the MNs. It is worth noting that while the aforementioned values provide a fair assessment of the printed needles' geometrical parameters, light microscopy systems used here were not optimised for measuring 3D objects (objects extending on Z-dimension). Inaccuracies associated with parallax effect and angle of projection could affect the accuracy of these figures. More accurate characterisation was conducted using volumetric imaging by means of μCT.

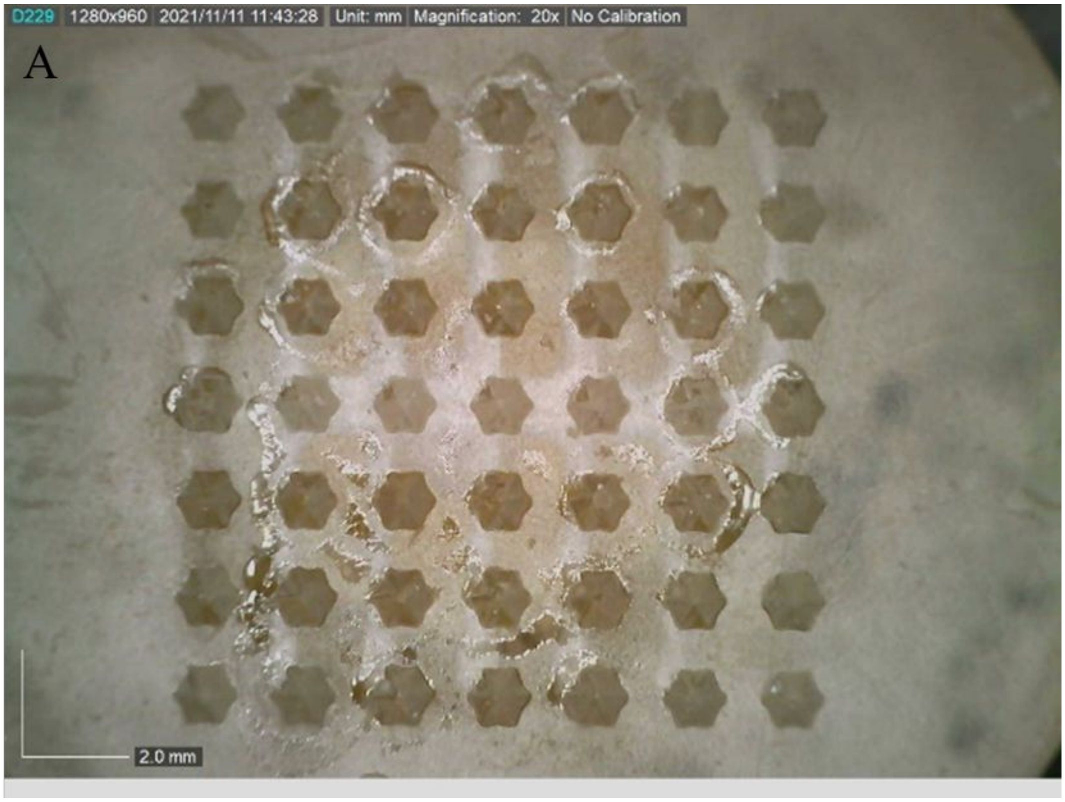
D229
1280x960
2021/11/11 11:43:28
Unit: mm
Magnification: 20x
No Calibration
A
2.0 mm


D233
1280x960
2021/11/11 11:54:44
Unit: mm
Magnification: 205x
No Calibration
B
L=0.119 mm
L=0.048 mm
L=0.692 mm
0.2 mm

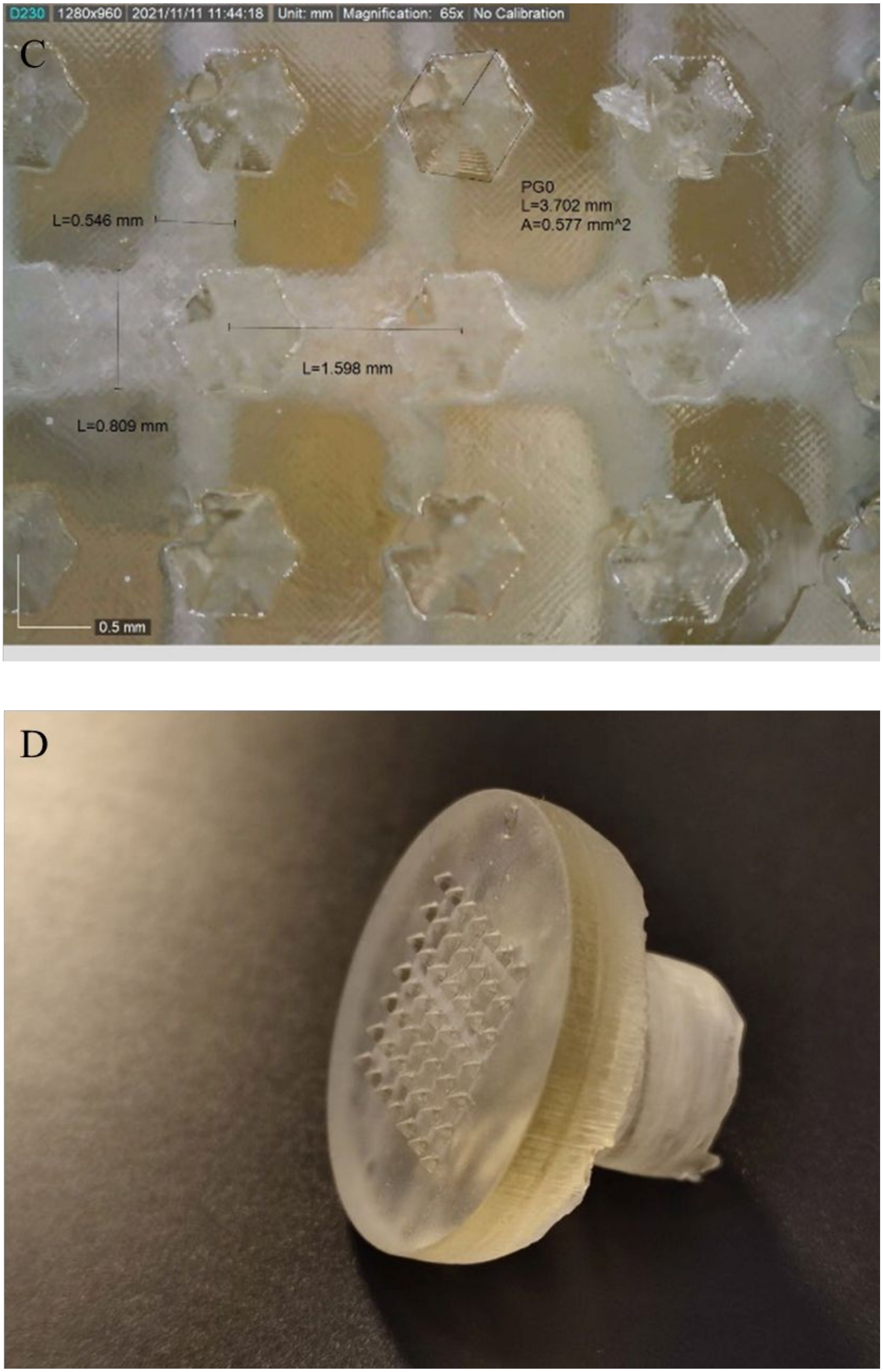
D230 1280x960 2021/11/11 11:44:18 Unit: mm Magnification: 65x No Calibration
C
PG0
L=3.702 mm
A=0.577 mm^2
L=0.546 mm
L=1.598 mm
L=0.809 mm
0.5 mm
D

Figure 1. Morphology of the printed hexagonal hollow MNs. **(A)** The array of the MNs (7x7), **(B)** the dimensions of the needle; height, and layer height, **(C)** the dimensions of the reservoir channels, and **(D)** the MN device with array I.

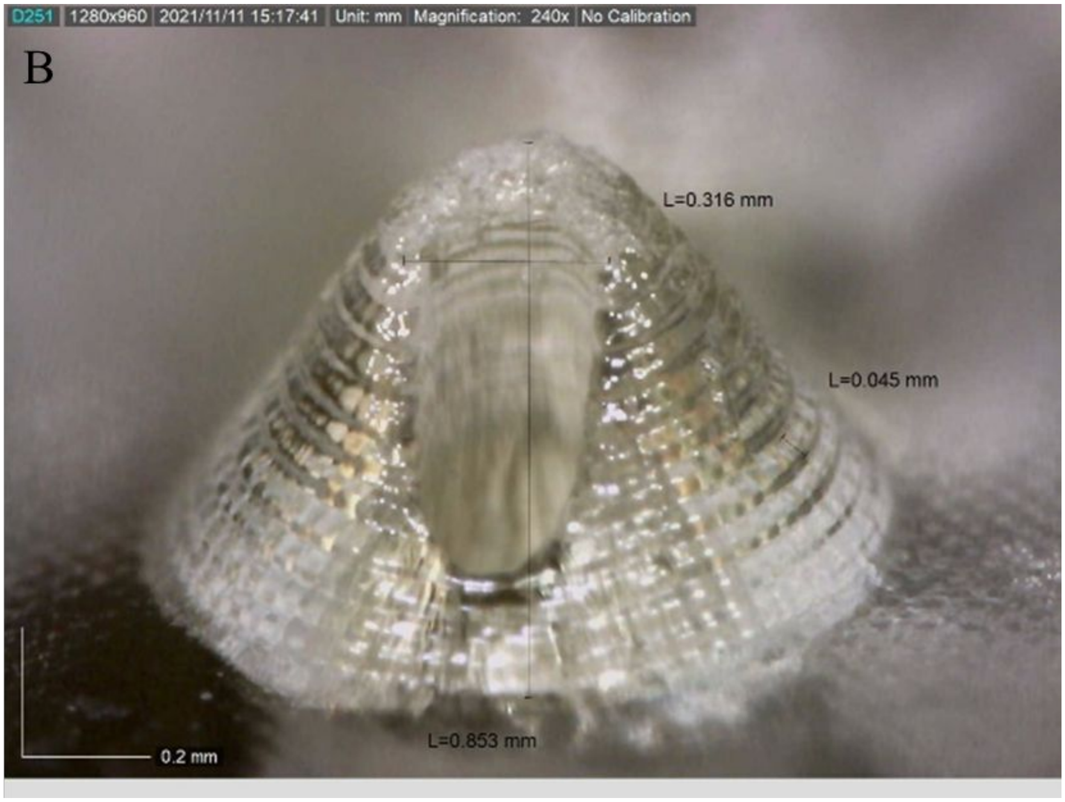
D251 1280x960 2021/11/11 15:17:41 Unit: mm Magnification: 240x No Calibration
B
L=0.316 mm
L=0.045 mm
L=0.853 mm
0.2 mm

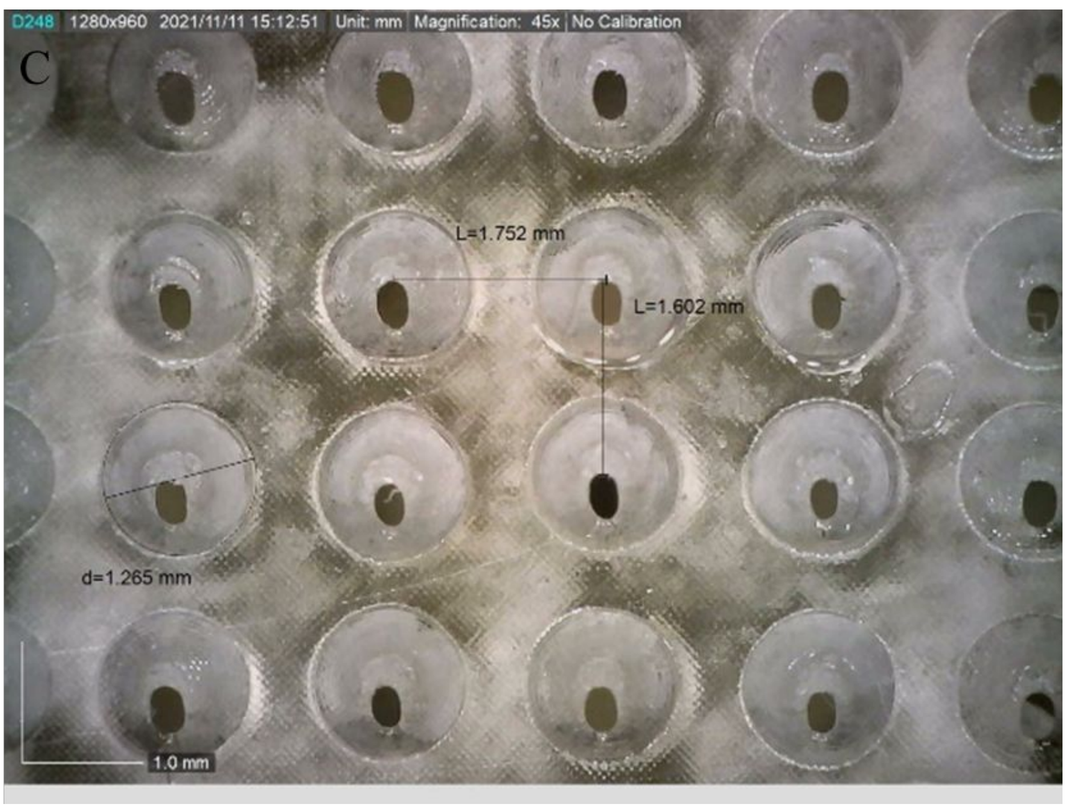
D248 1280x960 2021/11/11 15:12:51 Unit: mm Magnification: 45x No Calibration
C
L=1.752 mm
L=1.602 mm
d=1.265 mm
1.0 mm

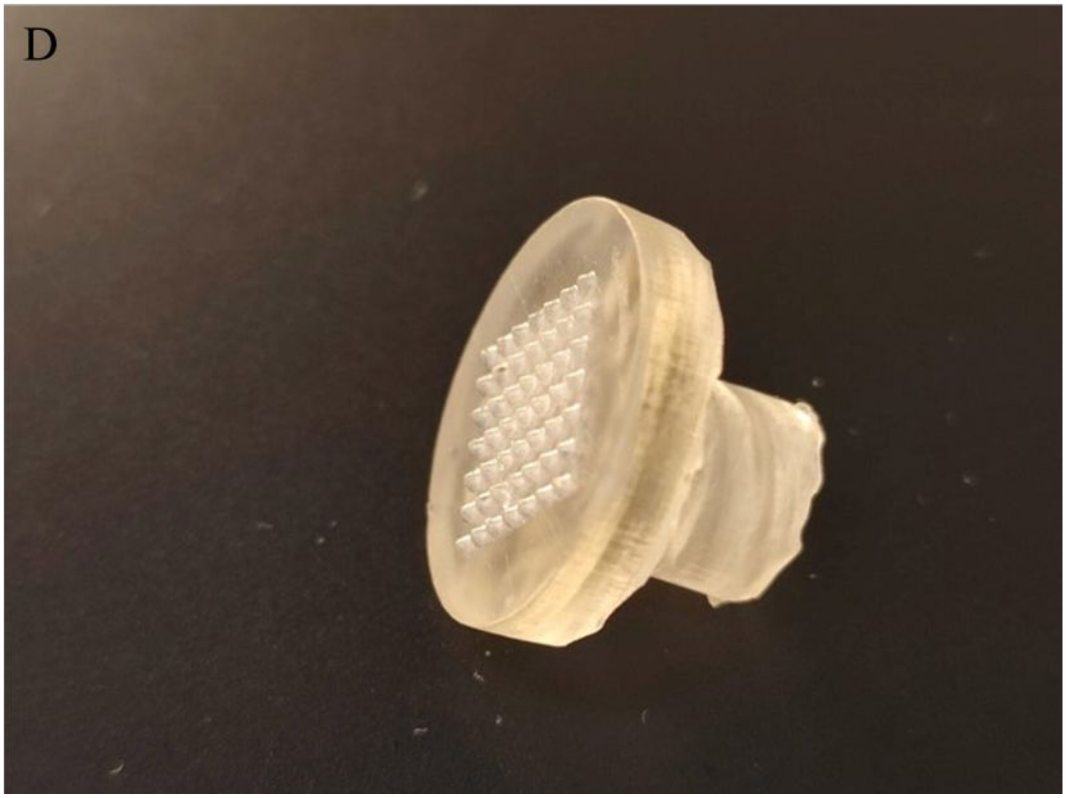

Figure 2. Morphology of the printed syringe like hollow MNs. **(A)** The array of the MNs (7x7), **(B)** dimension of a single needle; height, layer height, and the hole diameter, **(C)** dimensions of the MN array, and **(D)** the MN device with array II.

Volumetric characterisation by means of μCT

As per in the ‘microneedle design and fabrication’ section, all needles were designed to be 700 μm long. Our analysis of all 49 needles on both designs showed consistently shorter needle lengths which can be attributed to material shrinkage after curing. This shrinkage is owed to the shorter intermolecular distance of the molecules after polymerization[39]. Measured length from needle's base to the tip was 0.565 ± 0.032 mm and 0.570 ± 0.033 for the hexagonal (array I) and syringe-like (array II) needle arrays respectively. Length variation amongst needles of the same type was 6% for both needle geometries with values ranging [25^{th} – 75^{th} percentile] between 55 – 59 mm and 55 – 60 mm for array I and array II respectively.

The two geometries differed significantly in terms of needle volume, with array I (hexagonal) being 0.107 ± 0.009 mm^3 and array II (syringe-like) being 0.184 ± 0.019 mm^3, a difference of 71.9 %. This can be attributed to the open-lumen design of the hexagonal needles (Figure 3), which lacks excess material around the 2/3 of the lumen. This is also reflected by the measured surface area per needle, with the hexagonal geometry showing a surface area of 1.456 ± 0.081 mm^2 compared to 2.729 ± 0.186 mm^2 of the syringe-like ones (87.4 % difference).

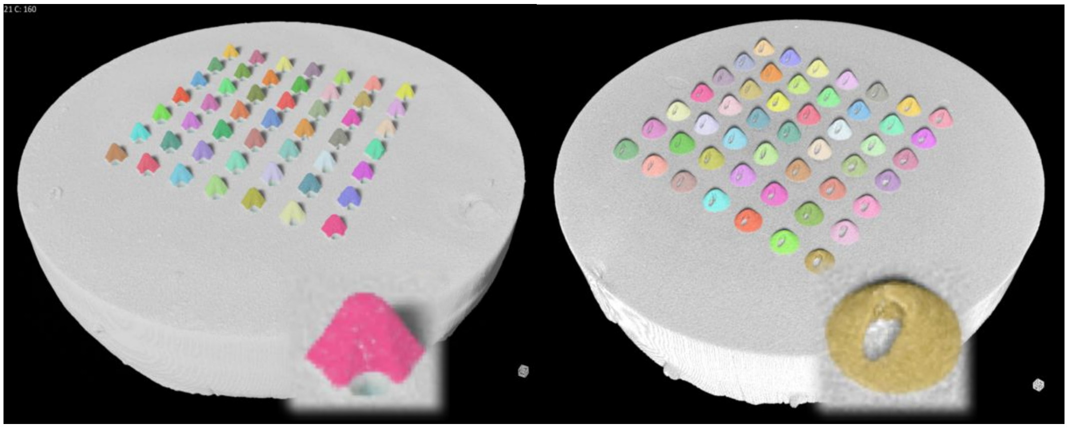

(A) **(B)**

Figure 3. 3D volume rendering of **(A)** the hexagonal (array I) and **(B)** syringe-like (array II) needle geometries. Close-ups of each geometry are showing in inserts. Individual needles rendered using different colours for clarity.

In terms of the fluid supply reservoir structure, the channel design used on the hexagonal needle arrays (array I) was more susceptible to printing imperfections and incomplete clearing contaminants (Figure 4).

272 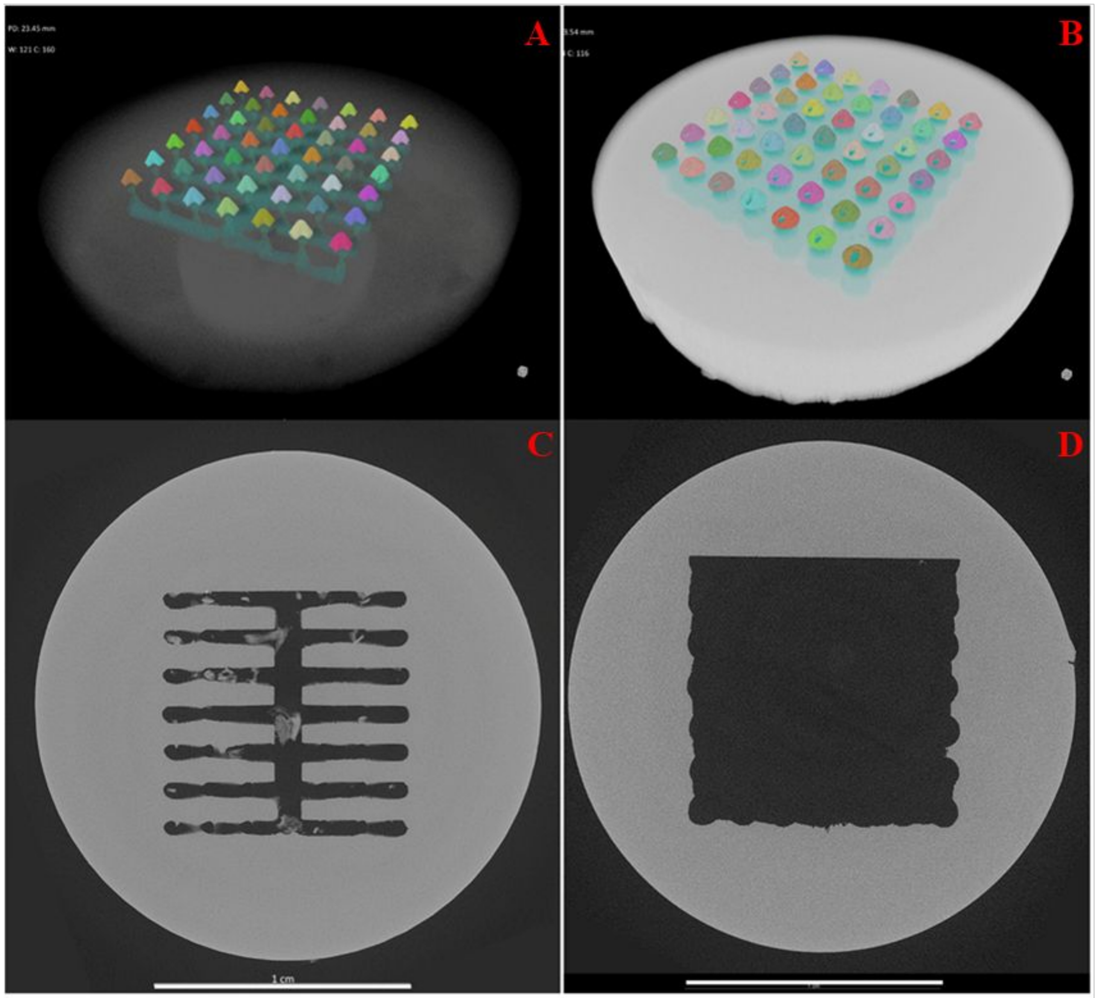

273 **Figure 4.** 3D volume rendering of the fluid supply reservoir rendered in turquoise of both array
274 designs (**A** and **B**) and single CT slice across the centre of the reservoir (**C** and **D**). Note the printing
275 imperfections such as channel narrowing and incomplete clearing contaminants within the
276 channels on the channel design of the hexagonal needle array. Scale bar at 10 mm.

277

278 **Mechanical properties**

The mechanical strength of hexagonal and syringe-like MNs was measured using a tensile test machine. Figure 5 depicts the results from the compression test conducted for array I and array I. Both arrays experienced forces greater than MN arrays face during insertion to the buccal mucosa [8]. As shown in Figure 5, hexagonal MNs can withstand forces up to 240 N and syringe-like MNs can bear up to 310 N. After that, both MNs are seriously damaged. Hexagonal MNs seem to tolerate less force than syringe-like MNs, in spite of the fact that they are made of the same resin. This is probably owed to the different shapes and needle tips of the two MNs. Studies have shown that the tip sharpness significantly influences the mechanical behavior of the MN structures[40]. The smaller tip diameter of the hexagonal MNs is presumably the reason for the lower mechanical strength. The MNs were evaluated after compression test using Scanning Electron Microscopy (SEM). Figure 5B depicts the hexagonal MNs after compression. Fragments are visible around the needle and the hole is almost closed due to compression of the needle. Figure 5C presents the syringe-like MNs after testing.

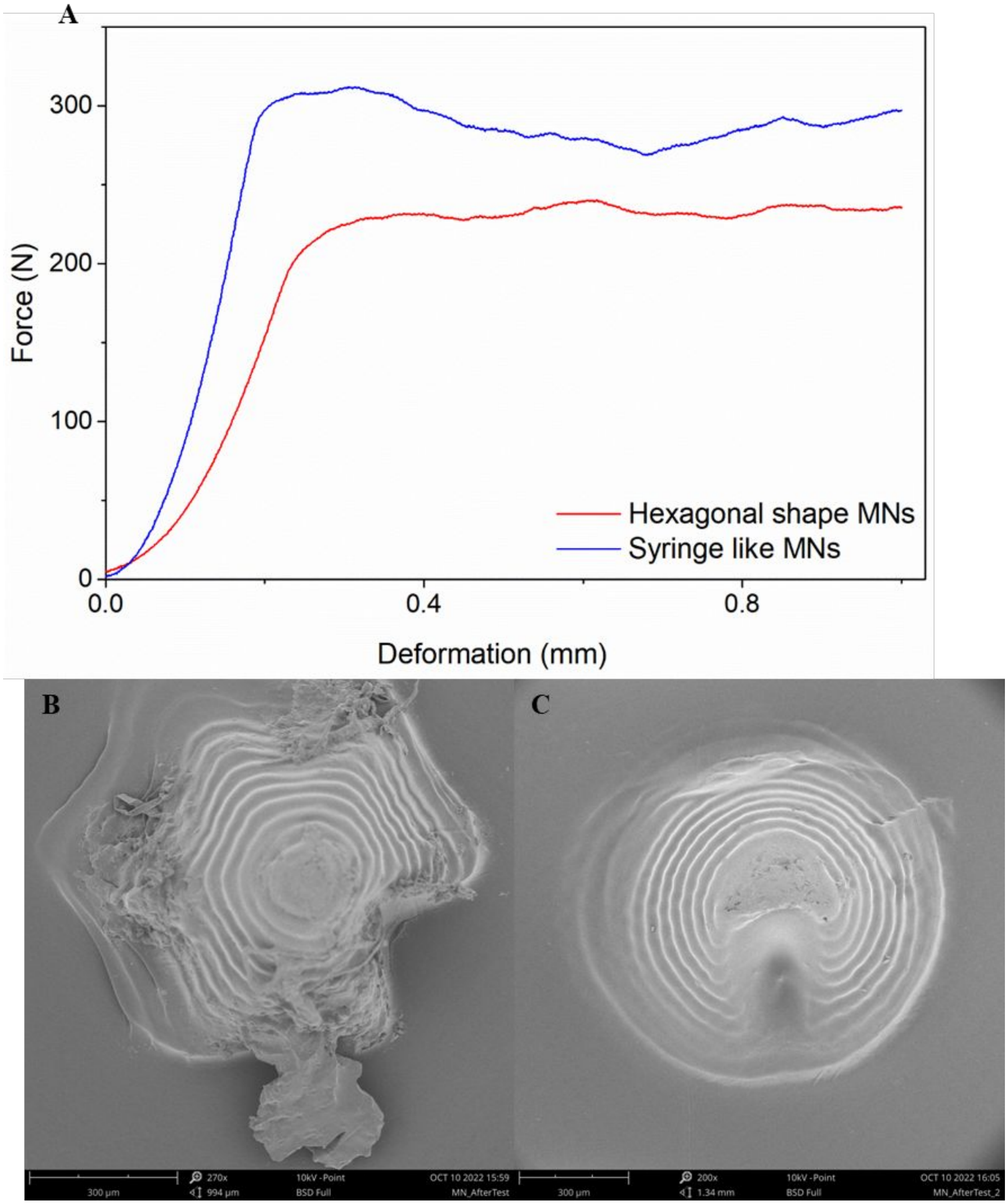
A
Force (N)
300
200
100
0
0.0
0.4
0.8
Deformation (mm)
Hexagonal shape MNs
Syringe like MNs
B
C
300 µm
270x
994 µm
10kV - Point
BSD Full
OCT 10 2022 15:59
MN_AfterTest
300 µm
200x
1.34 mm
10kV - Point
BSD Full
OCT 10 2022 16:05
MN_AfterTest_2

Figure 5. **(A)** Compression test of hexagonal and syringe-like MNs demonstrating force-displacement experimental data. SEM images after compression test of **(B)** hexagonal and **(C)** syringe-like MNs.

Penetration test and FEA simulations

The capability of the hollow MNs to perforate porcine buccal mucosa has been investigated through instrumented penetration tests, assisted by FEA simulations. The applied forces have been measured and compared between two different geometrical configurations of the MNs. In the first place, compression and nanoindentation mechanical testing techniques[41–43] were conducted to measure the mechanical properties of the 3D printed resin material. The compressive strength and the modulus were determined to be 122 ± 6 MPa and the elastic modulus 3099 MPa. FEA models have been introduced to improve the calculation accuracy of the forces applied during porcine buccal mucosa penetration tests and an explicit dynamics analysis was performed on ANSYS code. The thickness of the buccal mucosa layer was considered to be 700 μm since the average thickness has been reported to be 729 ± 95 μm[44]. Material failure and an evolving contact surface between MNs and target was introduced to define the insertion of the MN array and the surface of the buccal mucosa samples, which is governed by large deformations[24]. A material erosion algorithm was utilized to study the failure and separation of the material. The material erosion method removes distorted elements during the solution, i.e. along the MN trajectory, based upon material failure and separation due to fracturing of the surface of the buccal mucosa. Since the connective tissue is not involved with failure and significant deformation, the first two layers, epithelium and basal lamina, were modeled as hyperelastic materials[26,38]. Hyperelastic material models can be generally classified into two categories, mechanistic (micro-mechanical) and phenomenological (macro-mechanical)[45]. A hyperelastic material describes the stress–strain relationship using a continuous function rather than one or a series of elastic constants, generating a true nonlinear map of behavior[46]. Therefore, in this study, a first order Ogden material model was applied to replicate the exact mechanical behavior of buccal mucosa, in order to minimize the difference between the simulated and the experimental load-deformation curves.

The experimental setup of the buccal penetration process is shown in Figures 6A. The force-displacement responses for the MN configurations are demonstrated in Figure 6C. The results of simulations are shown in Figure 6C and accurately curve-fitted the experimental force-deformation data up to maximum force of 10 N. During the deformation phase, the force exponentially

325 increases as each MN is pressed against the buccal mucosa. The drops in the experimental force-
326 deformation curve may be explained by local perforation of a single MN prior piercing the buccal
327 mucosa from all MNs. Since the assumptions on the material parameters in the FEA model
328 returned results that fitted the experimental data, the hyperelastic material model parameters of the
329 buccal mucosa were considered optimal. These material model parameters returned a stress-strain
330 peak values of 1.05MPa and 78.75% strain. These results are in agreement with values from
331 literature [47]. Microscopy images of the MNs were taken after the penetration test to examine their
332 morphology (Figure 6D and 6E). Images show that there was a decrease in the needle length up to
333 30% for both hexagonal and syringe-like needles. The simulation of the penetration test revealed
334 that the stress concentration was located at the tip of the MNs, as displayed by the equivalent stress
335 results in Figure 7A and B This demonstrates the stress contouring of the FEA simulating the
336 behavior of the MN at the last step of the penetration test simulation. The maximum stress
337 experienced by the insertion process was calculated to be 33.6 MPa and 24.2 MPa for the hexagon
338 shaped and syringe-like configuration, respectively. There is no concern regarding the
339 concentration of the stress obtained at the tip area of the MN for both the configurations, since the
340 ultimate compressive strength was measured 122 ± 6 MPa, as mentioned previously.

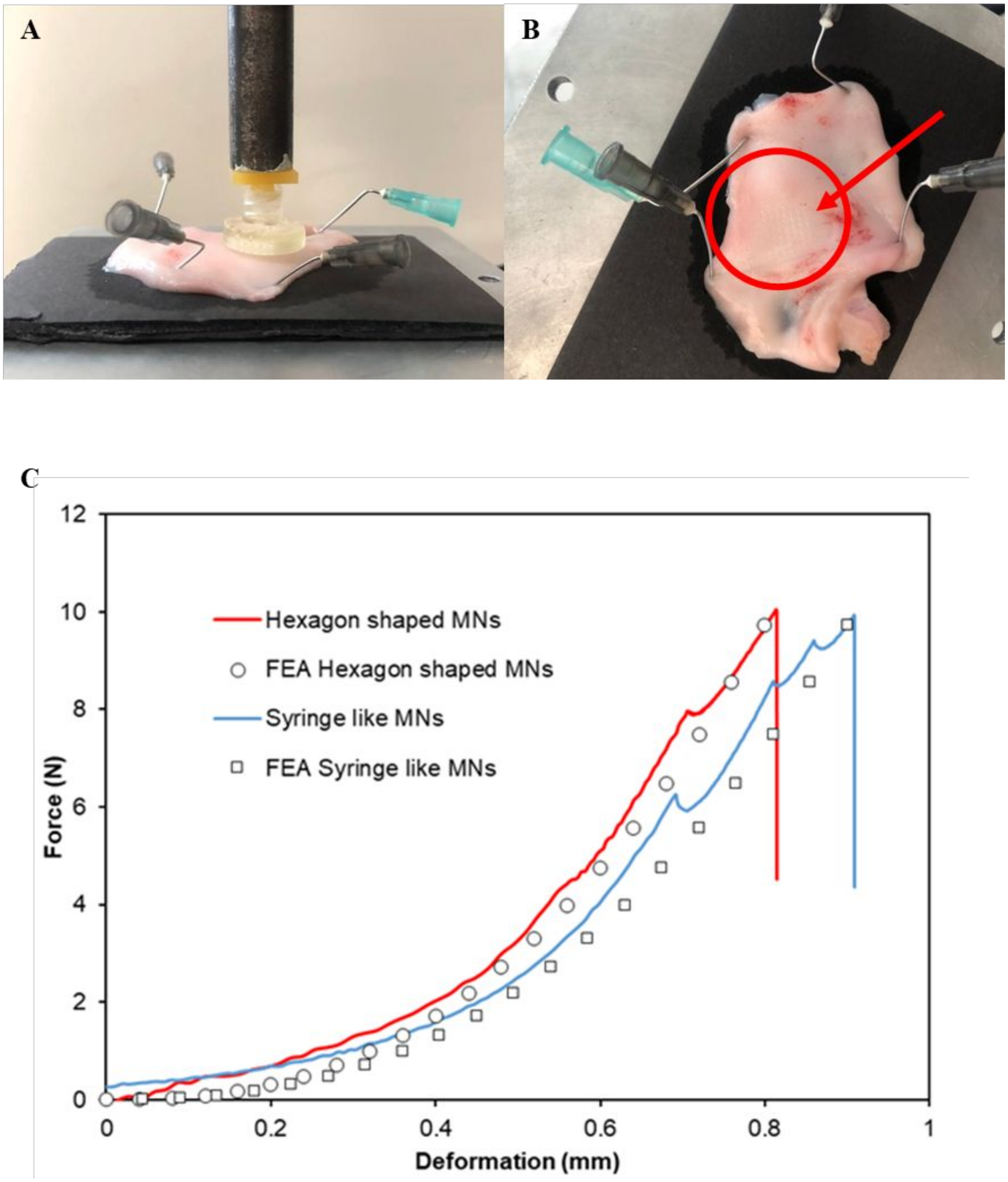
A
B
C
Hexagon shaped MNs
FEA Hexagon shaped MNs
Syringe like MNs
FEA Syringe like MNs
Force (N)
Deformation (mm)
0
2
4
6
8
10
12
0
0.2
0.4
0.6
0.8
1

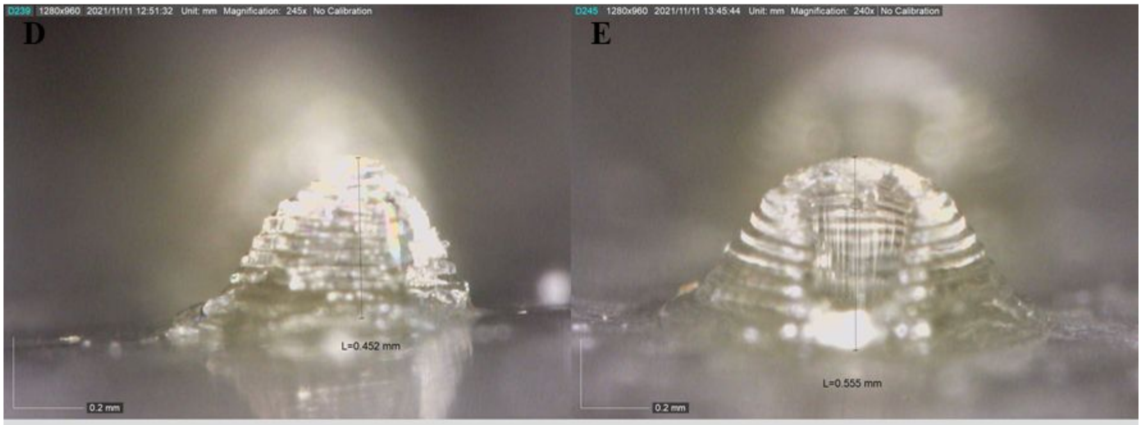

Figure 6. (A) Illustration of the penetration test using buccal mucosa, **(B)** the buccal mucosa after penetration showing the perforation sites, **(C)** force-deformation curve of both arrays fitted by FEA, **(D)** and **(E)** microscopy images of array I and array II respectively, after penetration test.

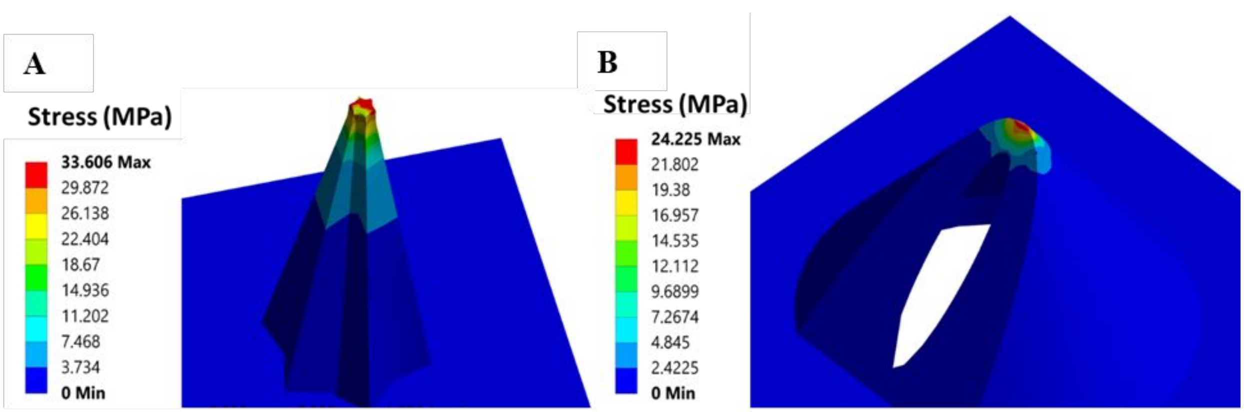

Figure 7. Stress distribution of **(A)** hexagon and **(B)** syringe-like hollow MN at the last step of the simulation of buccal mucosa penetration using FEA.

Permeation studies

Permeation studies were conducted using Franz diffusion cells. Porcine buccal mucosa was mounted between the donor and the acceptor, with the epithelium side facing the donor. The MN devices were connected to the syringe pumps and diffused the solutes across the buccal epithelium. Two different molecules namely FITC-dextran and calcein were tested to evaluate their permeability using the printed MN devices. Different flow rates were tested for pumping, namely 0.5, 0.2, 0.05 mL/min using FITC-Dextran 4.4 kDa as model compound. High flow rates resulted in leakage and in poor permeability for FITC-dextran as shown in Figure 8B. Previously, it has been reported that high volumes of injected liquids leak out from tissues causing a non-uniform distribution of the drug[33]. However, a flow rate of 0.05 mL/min led to higher permeability values and was further selected as the optimal flow rate for further evaluation of the MN devices. Both hexagonal and syringe-like needles pierced the buccal tissue for 30 and 60 sec and the results are depicted in Figure 8C and 8D. As evidenced from Figure 8C, FITC-dextran exhibited a two-fold increased permeability after piercing for 30 and 60 sec with both arrays, compared to the control group (t-test, $p<0.05$). Despite the large molecular weight of FITC-dextran (4000 Da), it can easily permeate across the membranes and its permeability is increased after MN insertion[48]. However, piercing for 60 sec does not show a significant increase in FITC's permeation neither for the MNs nor for the control group (t-test $p>0.05$). This can be attributed to the retraction of the MN devices immediately after piercing. It has been reported that the flow rate progressively increases with needle retraction[49] and as shown in Figure 8B, higher flow rates result in leakages. Thus, it is presumed that after 60 sec of piercing leakages occur that affect the permeation profile of FITC. Furthermore, findings suggest that fluid flow into tissue samples at a constant pressure, decreases over time[49], indicating that piercing time over 30 sec cannot increase the permeability of the model dye. The current results imply that the volume of the lumen [(array I (hexagonal) 0.107 mm^3 and array II (syringe-like) 0.184 mm^3], the structural features of the microneedles and the force displacement responses of these microneedles have little effect to the permeation of this dye across porcine epithelium and the increased transport is the due to flow rate in both cases. It appears that the permeation of FITC-Dextran 4kDa across the porcine epithelium is governed by the diffusion of the solute through the paracellular pathway which ultimately affect the transport rate of the active prevailing the other parameters. Previous studies have shown that comparable permeability values were obtained for FITC- Dextran 4 kDa and FITC-dextran 10 kDa as measured by flux studies across buccal epithelium suggesting paracellular transport of these solutes. The authors hypothesized that if the transport of the dyes would follow the transcellular pathway the differences in the permeability values would be more pronounced[50].

The picture was different for calcein transport studies across porcine epithelium. Calcein is a small hydrophilic molecule with poor permeability across cellular membranes and it is often used as a marker to examine *in vitro* the barrier integrity[51,52]. As shown in Figure 8D, no appreciable amounts of calcein were delivered by passive diffusion. Significantly higher transport rates compared to the control were obtained after piercing for 30 and 60 sec upon application of the syringe-like microneedles (array II) (t-test $p<0.05$) where the transport rate was increased 10 fold and 1000 fold respectively implying that piercing for longer time augment the solute to enter the perforation sites and finally permeate the tissue resulting to significantly higher permeation rates (t-test $p<0.05$) over time.

In a similar manner increased transport rates were observed upon application of hexagonal-like microneedles (array I) as a function of piercing time. Longer piercing time seem to facilitate the transport of calcein through the tissue, in contrast with the results for FITC-dextran. This is probably attributed to the lower molecular weight of calcein and the fact that it is transported across the epithelium through the holes created from the MNs. Array I also seem to have increased permeability for calcein in 30 sec compared to array II ($p < 0.05$), while after 60 sec the permeability for both arrays is approximately the same ($p > 0.05$). As shown previously in penetration test, the sharpness and the length of the needles is decreased after piercing the buccal tissue (Figure 6D and 6E). This deformation leads to similar transport values for calcein in 60 sec. In 30 sec, the needles seem to keep their integrity and differences in permeability values occur. Overall, these results show that both MN devices can significantly increase the permeability of both molecules after a short piercing time. In addition to that, the results demonstrate that these devices might be utilized for buccal delivery of actives with both high and low molecular weight thus increasing their permeability across buccal epithelium.

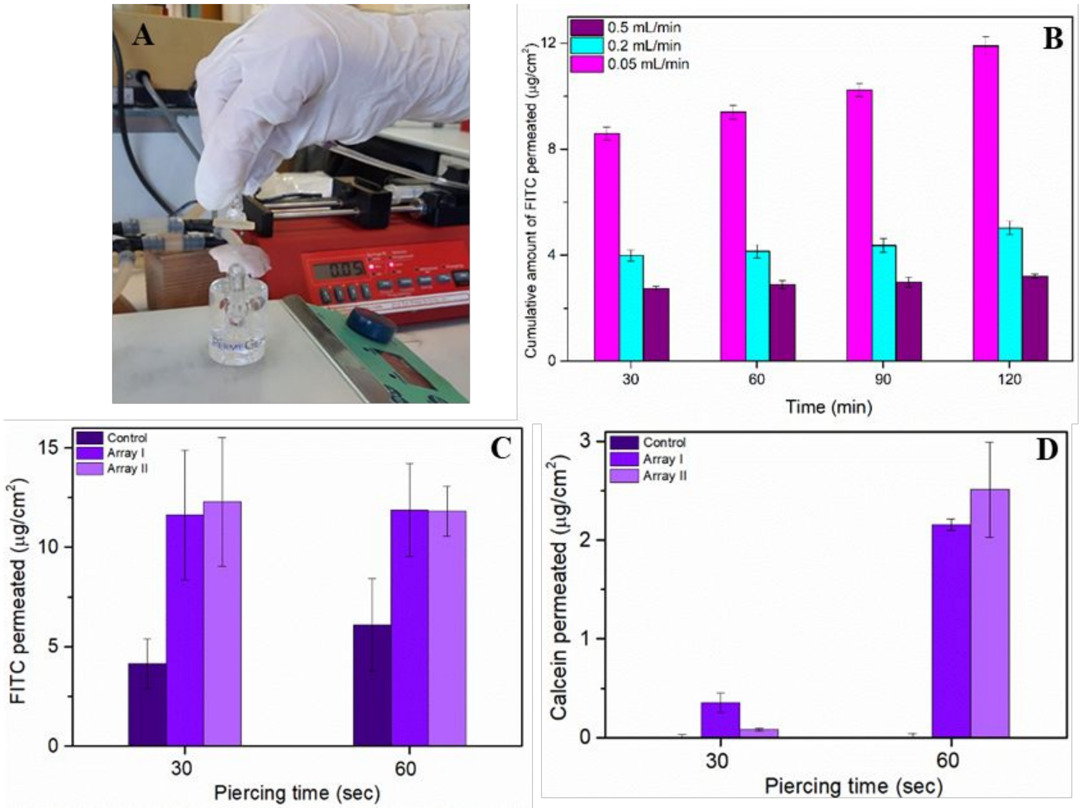

8/Figure 8. (A) Permeation study of the MN devices using Franz diffusion cells and syringe pump. The pump setting was 0.05 mL/min. **(B)** The cumulative amount of FITC permeated (µg/cm^2) with the three different flow rates. High flow rates resulted in leakages and poor permeation of FITC. **(C)** Cumulative amount of FITC and **(D)** calcein after piercing for 30 and 60 sec.

Histological evaluation

To confirm the safety of the MNs after piercing the porcine buccal mucosa, histological evaluation was conducted for both MN arrays, using hematoxylin-eosin staining. Figure 9 depicts the microscopy images after piercing the buccal tissue for 30 and 60 sec. Piercing for 30 sec revealed no damage to the mucosa while piercing for 60 sec showed a local epithelium detachment (Figure 9B), while a pattern of the MNs is visible in Figure 9D. These results show that the MN devices do not injure severely the buccal epithelium, which can recover from the MN piercing.

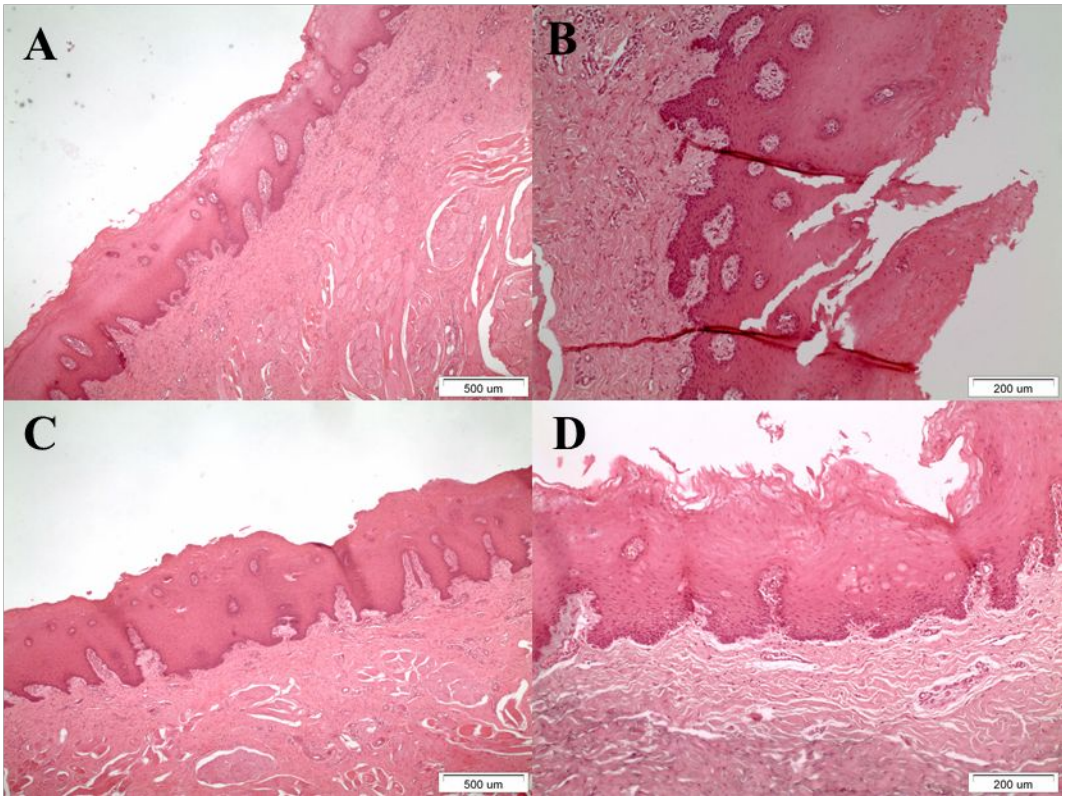

Figure 9. Histological evaluation after piercing with **(A)** array I for 30 sec, **(B)** array I for 60 sec, **(C)** array II for 30 sec, and **(D)** array II for 60 sec.

Cell viability

Viability studies of TR146 cells, following the application of liquid resin, printed films, and PBS extracts, are presented in Figure 10. No obvious cytotoxicity was observed upon incubation for

24h with the tested samples. Incubation of the cells with the printed films shows a small increase in cell growth, compared with the positive control, indicating the safety of the printed devices as buccal drug delivery systems. The presence of monomers did not have any cytotoxic effect, probably due to the short period of exposure (24h). These results confirmed the cytocompatibility of the commercial resin in TR146 cell cultures, which is a human cell line. In addition to that, MN devices are designed only for a few seconds administration to the buccal tissue suggesting that the printed devices are safe for buccal administration.

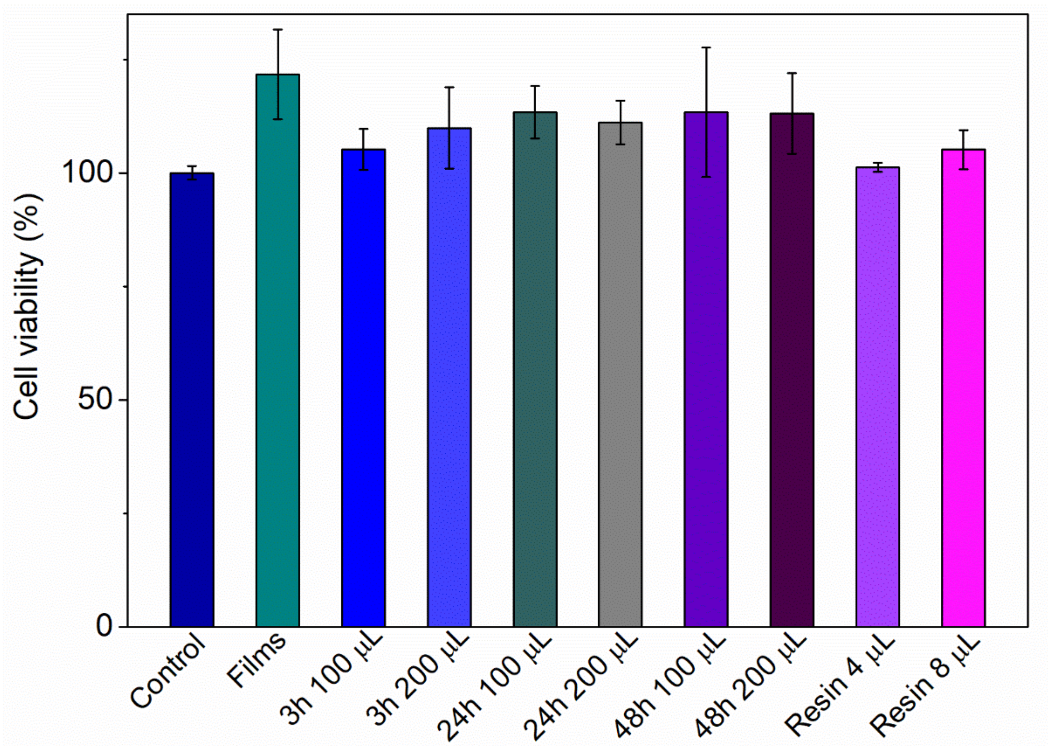

Figure 10. Assessment of cell viability (%) of TR146 cultures exposed to incubation for 24h with printed films, PBS cube extracts and liquid resin, as indicated above.

Conclusions

3D printed hollow MN devices were successfully fabricated using DLP printing. Two different shapes of needles were designed a conventional shape (syringe-like) and a hexagonal shape that it was firstly introduced in the present study. Both arrays had attached reservoirs designed with lumen for the hexagonal needles and a simple tank for the syringe-like needles. Microscopy studies showed the good printability of the material and the shape fidelity of the printed objects with their CAD model. The MNs were evaluated regarding their mechanical properties to ensure that they are able to pierce the buccal tissue without breaking and leaving fragments in the oral cavity that may result in toxicity. μCT studies provided a detail imaging of the MNs and their reservoirs with accurate dimensional characterization of the printed needles. Penetration test and FEA simulations confirmed the ability of the MNs to penetrate the buccal mucosa and permeability studies indicated that the printed devices could significantly increase the permeability of actives with high and low molecular weights. Moreover, the shape of the needles, the piercing time and the flow rate play a crucial role in the model dyes' permeability and needs to be further evaluated. In hollow MNs, the size and place of the pore is very important and requires a detail assessment regarding the piercing time into the tissue. Finally, histological and cell studies confirmed that the produced devices are safe and hold promise for the buccal administration of actives to special populations.

AUTHOR INFORMATION

Corresponding Author: Prof. Dimitrios G. Fatouros, e-mail: dfatouro@pharm.auth.gr

Present Addresses: Department of Pharmacy Division of Pharmaceutical Technology, Aristotle University of Thessaloniki, Thessaloniki 54124, Greece

Author Contributions

The manuscript was written through contributions of all authors. All authors have given approval to the final version of the manuscript.

ACKNOWLEDGMENTS

The authors acknowledge the μ-VIS X-ray Imaging Centre at the University of Southampton, founding partner of UK National Research Facility for lab-based X-ray Computed Tomography, for the provision of the μCT imaging facilities, data processing, and management infrastructure and expertise.

REFERENCES

(1) Wang, S.; Jiang, L.; Meng, S.; Liu, C.; Wang, H.; Gao, Z.; Guo, J. Hollow Mesoporous Silica Nanoparticles-Loaded Ion-Crosslinked Bilayer Films with Excellent Mechanical Properties and High Bioavailability for Buccal Delivery. *Int. J. Pharm.* **2022**, *624*, 122056.

(2) Sahatsapan, N.; Pamornpathomkul, B.; Rojanarata, T.; Ngawhirunpat, T.; Poonkhum, R.; Opanasopit, P.; Patrojanasophon, P. Feasibility of Mucoadhesive Chitosan Maleimide-Coated Liposomes for Improved Buccal Delivery of a Protein Drug. *J. Drug Deliv. Sci. Techn.* **2022**, *69*, 103173.

(3) Tran, P. H. L.; Duan, W.; Tran, T. T. D. Recent Developments of Nanoparticle-Delivered Dosage Forms for Buccal Delivery. *Int. J. Pharm.* **2019**, *571*, 118697.

(4) Eleftheriadis, G. K.; Monou, P. K.; Bouropoulos, N.; Boetker, J.; Rantanen, J.; Jacobsen, J.; Vizirianakis, I. S.; Fatouros, D. G. Fabrication of Mucoadhesive Buccal Films for Local Administration of Ketoprofen and Lidocaine Hydrochloride by Combining Fused Deposition Modeling and Inkjet Printing. *J. Pharm. Sci.* **2020**, *109* (9), 2757-2766.

(5) Zewail, M. B.; F.Asaad, G.; Swellam, S. M.; Abd-allah, S. M.; K.Hosny, S.; Sallah, S. K.; E.Eissa, J.; S.Mohamed, S.; El-Dakroury, W. A. Design, Characterization and in Vivo

Performance of Solid Lipid Nanoparticles (SLNs)-Loaded Mucoadhesive Buccal Tablets for Efficient Delivery of Lornoxicam in Experimental Inflammation. *Int. J. Pharm.* **2022**, *624*, 122006.

(6) Kraisit, P.; Hirun, N.; Mahadlek, J.; Limmatvapirat, S. Fluconazole-Loaded Solid Lipid Nanoparticles (SLNs) as a Potential Carrier for Buccal Drug Delivery of Oral Candidiasis Treatment Using the Box-Behnken Design. *J. Drug Deliv. Sci. Tech.* **2021**, *63*, 102437.

(7) Xu, J.; Strandman, S.; Zhu, J. X. X.; Barralet, J.; Cerruti, M. Genipin-Crosslinked Catechol-Chitosan Mucoadhesive Hydrogels for Buccal Drug Delivery. *Biomaterials* **2015**, *37*, 395-404.

(8) Oh, Y.-J.; Cha, H.-R.; Hwang, S. J.; Kim, D.-S.; Choi, Y.-J.; Kim, Y.-S.; Shin, Y.-R.; Nguyen, T. T.; Choi, S.-O.; Lee, J. M.; Park, J.-H. Ovalbumin and Cholera Toxin Delivery to Buccal Mucus for Immunization Using Microneedles and Comparison of Immunological Response to Transmucosal Delivery. *Drug Del.Trans. Res.* **2021**, *11* (4), 1390-1400.

(9) Caffarel-Salvador, E.; Kim, S.; Soares, V.; Tian, R. Y.; Stern, S. R.; Minahan, D.; Yona, R.; Lu, X.; Zakaria, F. R.; Collins, J.; Wainer, J.; Wong, J.; McManus, R.; Tamang, S.; McDonnell, S.; Ishida, K.; Hayward, A.; Liu, X.; Hubálek, F.; Fels, J.; Vegge, A.;

Frederiksen, M. R.; Rahbek, U.; Yoshitake, T.; Fujimoto, J.; Roxhed, N.; Langer, R.; Traverso, G. A Microneedle Platform for Buccal Macromolecule Delivery. *Sci. Adv.* **2021**, *7* (4), eabe2620.

(10) Lee, Y.; Li, W.; Tang, J.; Schwendeman, S. P.; Prausnitz, M. R. Immediate Detachment of Microneedles by Interfacial Fracture for Sustained Delivery of a Contraceptive Hormone in the Skin. *J. Control. Rel.* **2021**, *337*, 676-685.

(11) Choi, H.-J.; Yoo, D.-G.; Bondy, B. J.; Quan, F.-S.; Compans, R. W.; Kang, S.-M.; Prausnitz, M. R. Stability of Influenza Vaccine Coated onto Microneedles. *Biomaterials* **2012**, *33* (14), 3756-3769.

(12) Sabri, A. H. B.; Anjani, Q. K.; Utomo, E.; Ripolin, A.; Donnelly, R. F. Development and Characterization of a Dry Reservoir-Hydrogel-Forming Microneedles Composite for Minimally Invasive Delivery of Cefazolin. *Int. J. Pharm.* **2022**, *617*, 121593.

(13) Li, M.; Vora, L. K.; Peng, K.; Donnelly, R. F. Trilayer Microneedle Array Assisted Transdermal and Intradermal Delivery of Dexamethasone. *Int. J. Pharm.* **2022**, *612*, 121295.

(14) Waghule, T.; Singhvi, G.; Dubey, S. K.; Pandey, M. M.; Gupta, G.; Singh, M.; Dua, K. Microneedles: A Smart Approach and Increasing Potential for Transdermal Drug Delivery System. *Biomed Pharmacother.* **2019**, *109*, 1249-1258.

(15) Guillot, A. J.; Cordeiro, A. S.; Donnelly, R. F.; Montesinos, M. C.; Garrigues, T. M.; Melero, A. Microneedle-Based Delivery: An Overview of Current Applications and Trends. *Pharmaceutics* **2020**, *12* (6), E569.

(16) Economidou, S. N.; Douroumis, D. 3D Printing as a Transformative Tool for Microneedle Systems: Recent Advances, Manufacturing Considerations and Market Potential. *Adv. Drug Deliv. Rev.* **2021**, *173*, 60-69.

(17) Eleftheriadis, G. K.; Genina, N.; Boetker, J.; Rantanen, J. Modular Design Principle Based on Compartmental Drug Delivery Systems. *Adv Drug Deliv. Rev.* **2021**, *178*, 113921.

(18) Shin, D.; Hyun, J. Silk Fibroin Microneedles Fabricated by Digital Light Processing 3D Printing. *J. Ind. Eng. Chem.* **2021**, *95*, 126-133.

(19) Adamov, I.; Stanojević, G.; Medarević, D.; Ivković, B.; Kočović, D.; Mirković, D.; Ibrić, S. Formulation and Characterization of Immediate-Release Oral Dosage Forms with Zolpidem

Tartrate Fabricated by Digital Light Processing (DLP) 3D Printing Technique. *Int. J. Pharm.* **2022**, *624*, 122046.

(20) Zhang, J.; Hu, Q.; Wang, S.; Tao, J.; Gou, M. Digital Light Processing Based Three-Dimensional Printing for Medical Applications. *Int. J. Bioprint.* **2019**, *6* (1), 242.

(21) Evens, T.; Malek, O.; Castagne, S.; Seveno, D.; Van Bael, A. A Novel Method for Producing Solid Polymer Microneedles Using Laser Ablated Moulds in an Injection Moulding Process. *Manufactur. Letters* **2020**, *24*, 29-32.

(22) S.b.v.j., C.; Mannayee, G. Structural Analysis and Simulation of Solid Microneedle Array for Vaccine Delivery Applications. *Mater. Today Proc.* **2022**, *65*, 3774-3779.

(23) Economidou, S. N.; Uddin, Md. J.; Marques, M. J.; Douroumis, D.; Sow, W. T.; Li, H.; Reid, A.; Windmill, J. F. C.; Podoleanu, A. A Novel 3D Printed Hollow Microneedle Microelectromechanical System for Controlled, Personalized Transdermal Drug Delivery. *Add. Manufactur.* **2021**, *38*, 101815.

(24) Xenikakis, I.; Tzimtzimis, M.; Tsongas, K.; Andreadis, D.; Demiri, E.; Tzetzis, D.; Fatouros, D. G. Fabrication and Finite Element Analysis of Stereolithographic 3D Printed

Microneedles for Transdermal Delivery of Model Dyes across Human Skin in Vitro. *Eur. J. Pharm. Sci.* **2019**, *137*, 104976.

(25) Economidou, S. N.; Pere, C. P. P.; Reid, A.; Uddin, Md. J.; Windmill, J. F. C.; Lamprou, D. A.; Douroumis, D. 3D Printed Microneedle Patches Using Stereolithography (SLA) for Intradermal Insulin Delivery. *Mater Sci Eng C Mater Biol Appl.* **2019**, *102*, 743-755.

(26) Xenikakis, I.; Tsongas, K.; Tzimtzimis, E. K.; Katsamenis, O. L.; Demiri, E.; Zacharis, C. K.; Georgiou, D.; Kalogianni, E. P.; Tzetzis, D.; Fatouros, D. G. Transdermal Delivery of Insulin across Human Skin in Vitro with 3D Printed Hollow Microneedles. *J. Drug Del. Sci. Techn.* **2022**, *67*, 102891.

(27) Mathew, E.; Pitzanti, G.; Gomes dos Santos, A. L.; Lamprou, D. A. Optimization of Printing Parameters for Digital Light Processing 3D Printing of Hollow Microneedle Arrays. *Pharmaceutics* **2021**, *13* (11), 1837.

(28) Xing, J.-F.; Zheng, M.-L.; Duan, X.-M. Two-Photon Polymerization Microfabrication of Hydrogels: An Advanced 3D Printing Technology for Tissue Engineering and Drug Delivery. *Chem. Soc. Rev.* **2015**, *44* (15), 5031-5039.

(29) Moussi, K.; Bukhamsin, A.; Hidalgo, T.; Kosel, J. Biocompatible 3D Printed Microneedles for Transdermal, Intradermal, and Percutaneous Applications. *Adv. Eng.. Mater.* **2020**, *22* (2), 1901358.

(30) Gittard, S. D.; Ovsianikov, A.; Chichkov, B. N.; Doraiswamy, A.; Narayan, R. J. Two-Photon Polymerization of Microneedles for Transdermal Drug Delivery. *Expert Opin. Drug Deliv.* **2010**, *7* (4), 513-533.

(31) Di Carla Santos, S.; Fávaro-Moreira, N. C.; Abdalla, H. B.; Augusto, G. G. X.; Costa, Y. M.; Volpato, M. C.; Groppo, F. C.; Gill, H. S.; Franz-Montan, M. A Crossover Clinical Study to Evaluate Pain Intensity from Microneedle Insertion in Different Parts of the Oral Cavity. *Int. J. Pharm.* **2021**, *592*, 120050.

(32) Daly, S.; Claydon, N. C. A.; Newcombe, R. G.; Seong, J.; Addy, M.; West, N. X. Randomised Controlled Trial of a Microneedle Patch with a Topical Anaesthetic for Relieving the Pain of Dental Injections. *J. Dent.* **2021**, *107*, 103617.

(33) Ma, Y.; Boese, S. E.; Luo, Z.; Nitin, N.; Gill, H. S. Drug Coated Microneedles for Minimally-Invasive Treatment of Oral Carcinomas: Development and in Vitro Evaluation. *Biomed Microdevices.* **2015**, *17* (2), 44.

(34) Wang, T.; Zhen, Y.; Ma, X.; Wei, B.; Li, S.; Wang, N. Mannosylated and Lipid A-Incorporating Cationic Liposomes Constituting Microneedle Arrays as an Effective Oral Mucosal HBV Vaccine Applicable in the Controlled Temperature Chain. *Colloids Surf. B Biointerfaces*. **2015**, *126*, 520-530.

(35) Karavasili, C.; Eleftheriadis, G. K.; Gioumouxouzis, C.; Andriotis, E. G.; Fatouros, D. G. Mucosal Drug Delivery and 3D Printing Technologies: A Focus on Special Patient Populations. *Adv Drug Deliv Rev* **2021**, *176*, 113858.

(36) Li, X.-J.; Li, Y.; Meng, Y.; Pu, X.-Q.; Qin, J.-W.; Xie, R.; Wang, W.; Liu, Z.; Jiang, L.; Ju, X.-J.; Chu, L.-Y. Composite Dissolvable Microneedle Patch for Therapy of Oral Mucosal Diseases. *Biomat. Adv.* **2022**, *139*, 213001.

(37) Schindelin, J.; Rueden, C. T.; Hiner, M. C.; Eliceiri, K. W. The ImageJ Ecosystem: An Open Platform for Biomedical Image Analysis. *Mol. Reprod. Dev.* **2015**, *82*, 518-529

(38) Xenikakis, I.; Tsongas, K.; Tzimtzimis, E. K.; Zacharis, C. K.; Theodoroula, N.; Kalogianni, E. P.; Demiri, E.; Vizirianakis, I. S.; Tzetzis, D.; Fatouros, D. G. Fabrication of Hollow Microneedles Using Liquid Crystal Display (LCD) Vat Polymerization 3D Printing Technology for Transdermal Macromolecular Delivery. *Int. J. Pharm.* **2021**, *597*, 120303.

(39) Zhang, Q.; Weng, S.; Hamel, C. M.; Montgomery, S. M.; Wu, J.; Kuang, X.; Zhou, K.; Qi, H. J. Design for the Reduction of Volume Shrinkage-Induced Distortion in Digital Light Processing 3D Printing. *Extr. Mech. Letters* **2021**, *48*, 101403.

(40) Faraji Rad, Z.; Prewett, P. D.; Davies, G. J. Parametric Optimization of Two-Photon Direct Laser Writing Process for Manufacturing Polymeric Microneedles. *Additive Manufact.* **2022**, *56*, 102953.

(41) Mansour, M.; Tsongas, K.; Tzetzis, D.; Antoniadis, A. Mechanical and Dynamic Behavior of Fused Filament Fabrication 3D Printed Polyethylene Terephthalate Glycol Reinforced with Carbon Fibers. *Polymer-Plastics Techn. Eng.* **2018**, *57* (16), 1715-1725.

(42) Tzetzis, D.; Tsongas, K.; Mansour, G. Determination of the Mechanical Properties of Epoxy Silica Nanocomposites through FEA-Supported Evaluation of Ball Indentation Test Results. *Mater. Res.* **2017**, *20*, 1571-1578.

(43) Mansour, M.; Tsongas, K.; Tzetzis, D. Measurement of the Mechanical and Dynamic Properties of 3D Printed Polylactic Acid Reinforced with Graphene. *Polymer-Plastics Tech. Mater.* **2019**, *58* (11), 1234-1244.

(44) Meng-Lund, E.; Marxen, E.; Pedersen, A. M. L.; Müllertz, A.; Hyrup, B.; Holm, R.; Jacobsen, J. Ex Vivo Correlation of the Permeability of Metoprolol Across Human and Porcine Buccal Mucosa. *J. Pharm. Sci.* **2014**, *103* (7), 2053-2061.

(45) Steinmann, P.; Hossain, M.; Possart, G. Hyperelastic Models for Rubber-like Materials: Consistent Tangent Operators and Suitability for Treloar's Data. *Arch. Appl. Mech.* **2012**, *82* (9), 1183-1217.

(46) Chen, J.; Ahmad, R.; Li, W.; Swain, M.; Li, Q. Biomechanics of Oral Mucosa. *J. R. Soc. Interface.* **2015**, *12* (109), 20150325.

(47) Goktas, S.; Dmytryk, J. J.; McFetridge, P. S. Biomechanical Behavior of Oral Soft Tissues. *J. Periodontol.* **2011**, *82* (8), 1178-1186.

(48) Salamat-Miller, N.; Chittchang, M.; Johnston, T. P. The Use of Mucoadhesive Polymers in Buccal Drug Delivery. *Adv. Drug Deliv. Rev.* **2005**, *57* (11), 1666-1691.

(49) Martanto, W.; Moore, J. S.; Kashlan, O.; Kamath, R.; Wang, P. M.; O'Neal, J. M.; Prausnitz, M. R. Microinfusion Using Hollow Microneedles. *Pharm. Res.* **2006**, *23* (1), 104-113.

(50) Hoogstraate, A.J; Cullander, C.; Nagelkerke, J.F.; Senel, S.; Verhoef, J.C.; Junginger, H.E.; Boddé, H.E. Diffusion rates and transport pathways of fluorescein isothiocyanate (FITC)-labeled model compounds through buccal epithelium. *Pharm. Res.*, **1994** *11*(1):83-89.

(51) Macedo, A. S.; Castro, P. M.; Roque, L.; Thomé, N. G.; Reis, C. P.; Pintado, M. E.; Fonte, P. Novel and Revisited Approaches in Nanoparticle Systems for Buccal Drug Delivery. *J. Control. Rel.* **2020**, *320*, 125-141. https://doi.org/10.1016/j.jconrel.2020.01.006.

(52) Bibi, H. A.; di Cagno, M.; Holm, R.; Bauer-Brandl, A. Permeapad™ for Investigation of Passive Drug Permeability: The Effect of Surfactants, Co-Solvents and Simulated Intestinal Fluids (FaSSIF and FeSSIF). *Int. J. Pharm* **2015**, *493* (1), 192-197. https://doi.org/10.1016/j.ijpharm.2015.07.028.

Table of Contents

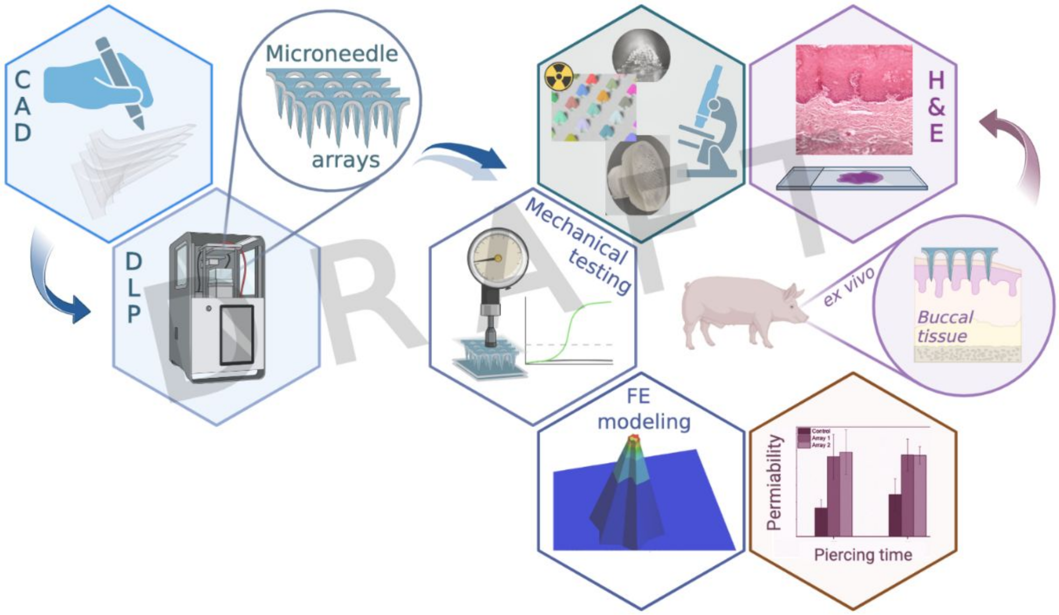
CAD
Microneedle
arrays
DLP
Mechanical
testing
H
&
E
ex vivo
Buccal
tissue
FE
modeling
Permiability
Control
Array 1
Array 2
Piercing time
DRAFT